ChemComm

COMMUNICATION

View Article Online
View Journal | View Issue

Cite this: *Chem. Commun.*, 2026, 62, 4363

Received 18th December 2025,
Accepted 26th January 2026

DOI: 10.1039/d5cc07128c

rsc.li/chemcomm

Facile construction of a covalent triazine framework as an anode for ultra-long cycle life sodium-ion batteries

Ying Huang,†[a] Suping Chen,†[a] Tao Yang,[a] Xijun Xu,*[a] Fangkun Li,[b] Jujun Yuan,*[c] Sihuan Tang,[a] Yanping Huo[ad] and Jun Liu*[b]

A covalent triazine framework (CTF) was synthesized *via* a typical solution synthesis route and applied as an anode for sodium-ion batteries (SIBs). The extended conjugate structure of CTF not only endows structural stability and limited solubility, but also improves electronic conductivity and offers numerous active sites. Meanwhile, the CTF displays a Na^+ storage capacity of 82.6 mAh g^{-1} after 9000 cycles at 2.0 A g^{-1}, indicating a superior long-term cycling stability. The $Na_3V_2(PO_4)_3$//CTF full cell demonstrates a capacity of 57.6 mAh g^{-1} after 1500 cycles at 1.0 A g^{-1}.

Sodium-ion batteries (SIBs) have demonstrated irreplaceable potential in large-scale energy storage and low-speed electric vehicles due to their abundant reserves (with Na constituting ~2.36% of the Earth's crust, significantly higher than Li's 0.0065%), widespread distribution, and cost-effectiveness, serving as a crucial complement to lithium-ion batteries (LIBs).[1–3] However, the larger radius of Na^+ (1.02 Å) compared to Li^+ (0.76 Å) results in greater resistance to intercalation/deintercalation and slower diffusion rates within electrode materials, which may cause structural degradation and subsequent capacity decay and cycling stability issues.[4–7] Furthermore, due to the limited interlayer spacing of conventional graphite anodes, Na^+ with a larger radius is unable to form stable Na^+ intercalation compounds.[8–10] Therefore, developing anode materials with high capacity, rapid ion transport rates, and structural stability remains a critical requirement for advancing the industrialization of SIBs.[11,12]

Current research on anode materials for SIBs primarily focuses on carbon-based materials, alloy-based materials, transition metal compounds, and organic materials.[13–19] While carbon-based materials (*e.g.*, hard carbon) demonstrate stable cycling performance, they exhibit low theoretical capacity.[9,20] Alloy-based materials (*e.g.*, Bi, Sb) offer higher capacity but suffer from significant volume expansion (>300%) and poor cycling stability.[13,14] Transition metal compounds (*e.g.*, metal oxides, sulfides) face challenges such as poor conductivity and structural collapse during cycling.[15] Organic materials have emerged as a research hotspot in recent years due to their advantages in designable molecular structures, renewable resources, and high theoretical capacity.[16–19] Among these, covalent organic frameworks (COFs), crystalline porous materials formed by covalent bonding of light elements (C, H, O, N), possess distinct crystalline structures, high specific surface areas, tunable pore sizes, and excellent chemical stability.[21–26] These properties provide a novel platform for addressing structural stability and ion transport challenges in SIB system. Among them, covalent triazine frameworks (CTFs) have garnered significant attention in energy storage applications owing to the triazine ring's (C_3N_3) strong electronic conjugation, high nitrogen content, and excellent chemical stability.[26,27] The nitrogen atoms within the triazine ring provide abundant active sites for Na^+ storage through adsorption–desorption or redox reactions. Additionally, the robust conjugated structure facilitates rapid electron transfer, enhancing the material's conductivity.[27,28]

Herein, a covalent triazine-based framework was fabricated as an anode material for SIBs. The extended conjugate structure endows CTF with exceptional structure stability and limited solubility in electrolytes. Consequently, the CTF displays a high specific capacity of 82.6 mAh g^{-1} after 9000 cycles at 2.0 A g^{-1}, indicating a superior long-term cycling stability. Detailed kinetic analysis indicates that the conjugate structure of CTF not only improves electronic conductivity but also offers numerous active sites for Na^+ storage. Meanwhile, the assembled $Na_3V_2(PO_4)_3$//CTF full cell demonstrates a high capacity of 57.6 mAh g^{-1} after 1500 cycles at 1.0 A g^{-1}. This work provides

[a] *School of Chemical Engineering and Light Industry, Guangdong University of Technology, Guangzhou, 510006, P. R. China. E-mail: xuxijun2022@gdut.edu.cn*
[b] *Guangdong Provincial Key Laboratory of Advanced Energy Storage Materials, School of Materials Science and Engineering, South China University of Technology, Guangzhou 510641, P. R. China. E-mail: msjliu@scut.edu.cn*
[c] *School of Intelligent Manufacturing and Future Energy, Gannan Normal University, Ganzhou 341000, China. E-mail: yuanjujun@gnnu.edu.cn*
[d] *Analytical&Testing Center, Guangdong University of Technology, Guangzhou, 510006, P. R. China*
† These authors contributed equally to this work.

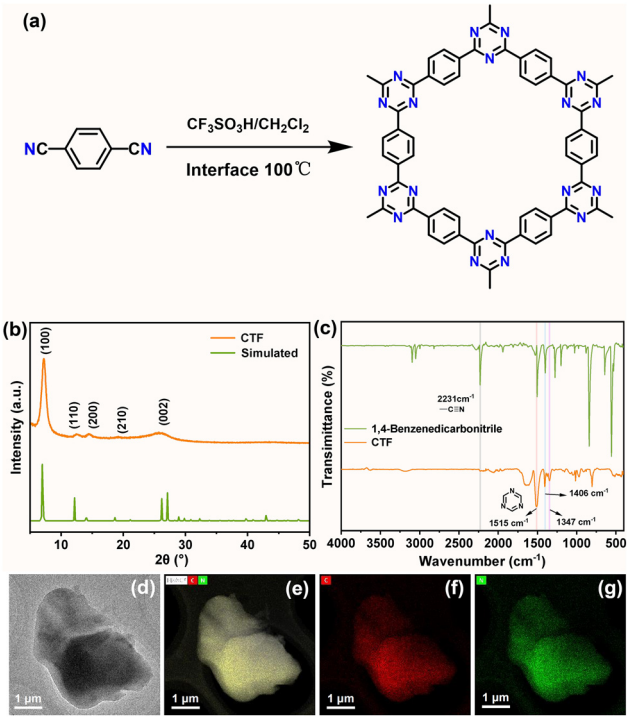

Fig. 1 (a) A schematic of the solution synthesis of CTF, (b) the XRD pattern of CTF and the simulated one, and (c) the FTIR spectra of CTF. (d) The TEM images and (e–g) corresponding EDX signals: (e) comprehensive element distribution, (f) C and (g) N, respectively.

valuable insights into designing high-performance organic anode materials for SIBs.

As illustrated in Fig. 1a, the CTF was fabricated by a facile solution synthesis *via* trimerization of carbonitrile.[29] The crystal structure information of the organic CTF was analyzed by an X-ray diffraction (XRD) instrument. As depicted in Fig. 1b, the main XRD peaks of the sample are ascribed to the (100), (110), (200), (210), and (002) crystal planes of CTF, respectively.[30,31] Fig. 1c exhibits the Fourier transform infrared (IR) spectra of the product CTF and the raw material 1,4-benzenedicarbonitrile. Apparently, the intrinsic peak of –CN located at 2231 cm^{-1} disappeared after the solution synthesis reaction. Furthermore, the peaks located at 1406 and 1347 cm^{-1} can be indexed to the triazine group, respectively.[32–35] The thermogravimetric analysis curve of CTF under an argon atmosphere (Fig. S1) exhibits two distinct weight loss stages: a slight weight loss (~5%) occurs below 600 °C, which is mainly attributed to the removal of adsorbed water and residual solvents, demonstrating good thermal stability. Subsequently, a significant weight loss (~30%) occurs from 600 °C to 900 °C, originating from the thermal decomposition of the conjugated triazine-based skeleton of CTF. Furthermore, the CTF possesses a typical mesoporous structure, with a specific surface area of 1320.0393 m^2 g^{-1} and a pore size of 3.78 nm (Fig. S2), which could provides abundant active sites for Na^+ adsorption and facilitates Na^+ diffusion. The scanning electron microscopy (SEM) images (Fig. S3) reveal the CTF with an irregularly agglomerated shape. The detailed morphology of CTF was further investigated *via* transmission electron microscopy (TEM). As depicted in Fig. 1d, the TEM results indicate that CTF has a plate shape with sizes of several micrometers. Furthermore, the EDX-mapping results of comprehensive elements, and the C and N element signals (Fig. 1e–g) indicate their co-existence within the plate-shaped particles.

To evaluate the Na^+ storage properties of the CTF anode, cyclic voltammetry (CV) and galvanostatic discharging/charging measurements were carried out. In the initial curve, the distinct cathodic peaks are assigned to the reduction reaction of CTF with Na^+, accompanied by the formation of the solid electrolyte interface (SEI) layer (Fig. S4).[36] The cathodic peaks at 0.87, 0.45 and 0.05 V and the anodic peaks at 0.1, 0.5 and 0.9 V on the 2nd to 5th profiles are attributed to the sodiation and desodiation procedures, respectively.[34,36,37] The subsequent CV profiles were well overlapped without obvious fluctuation, indicating good reversibility and stability of CTF for SIBs.[36,38] Fig. 2a depicts the initial five voltage-capacity curves for CTF at 0.1 mA g^{-1}, revealing an initial coulombic efficiency (ICE) of 85.9% with a discharge/charge capacity of 193.5/166.3 mAh g^{-1}. As depicted in Fig. 2b and S5, the CTF anode cycled at 0.1 A g^{-1} over 500 cycles retains a reversible capacity of 123.9 mAh g^{-1}. Fig. 2c exhibits a specific capacity of 156.8, 141.2, 133.9, 129.0, and 124.9 mAh g^{-1} as the charging/discharging current density increases from 0.1 to 2.0 A g^{-1}, respectively. Fig. 2d displays stable cycling behaviors from 0.1 to 2.0 A g^{-1} and returns to 136.8 mAh g^{-1} at 0.1 A g^{-1}, indicating superior rate capability of the CTF anode. The cycling behavior of CTF under high current densities of 1.0 and 2.0 A g^{-1} is also measured. As depicted in Fig. S6, the organic CTF anode cycled at 1.0 A g^{-1} over 1000 cycles maintains a capacity of 105.9 mAh g^{-1}.

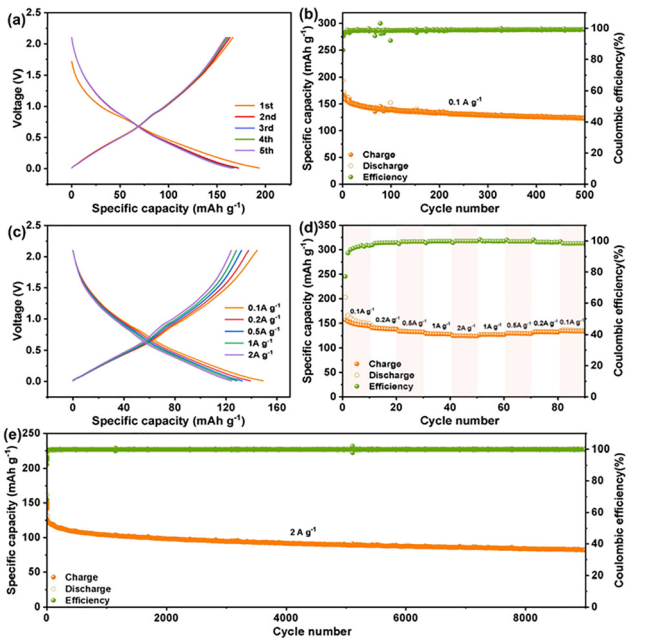

Fig. 2 Na^+ storage performance of CTF anodes: (a) initial five charge–discharge profiles and (b) cycling performance at 0.1 A g^{-1}. (c) Charge–discharge curves and (d) rate capabilities from 0.1 to 2.0 A g^{-1}. (f) Long-term cycling performance at 2.0 A g^{-1}.

Notably, the CTF anode at 2.0 A g^{-1} maintained a sustainable 82.6 mAh g^{-1} over 9000 cycles (Fig. 4f and Fig. S7). As exhibited in Table S1, this CTF exhibits superior cycling stability compared to other reported COF anodes for Na-ion storage.

To evaluate the kinetics of the CTF anode, CV tests were performed with the scan rate rising from 0.1 to 1.0 mV s^{-1}. As displayed in Fig. 2a, the CV profiles depict intrinsic anodic/cathodic peaks and preserve similar shapes upon different scan rates. Based on Dunn's empirical formula of $i = av^b$, the a and b are empirical parameters; the b-value could be calculated by linear fitting of log(i) and log(v) at the redox peaks.[39,40] As depicted in Fig. 3b, the b-value of O1, O2, O3, R1, R2, and R3 for CTF is calculated to be 1.06, 1.10, 1.08, 1.05, 1.10, and 0.91, respectively.[39,40] This data strongly supports that the interfacial and superficial pseudocapacitive behaviors dominated the entire cycle process, resulting in excellent rate capability.[39,40] Furthermore, the galvanostatic intermittent titration (GITT) during discharging/charging was performed to calculate the Na^+ diffusion coefficient of the CTF anode (Fig. 3c). It can be observed that the diffusion coefficient of Na^+ within CTF is $\sim 10^{-11}$ cm s^{-1}. This can be ascribed to the unique conjugate structure of CTF, which enhances the electroconductivity and endows sufficient pathways for Na^+ diffusion, thus further explaining the favourable rate capability.[41,42] To further understand the Na^+ diffusion behavior of the CTF anode, an *in situ* electrochemical impedance spectroscopy (EIS) test was also performed to explore the impedance evolution during initial cycles (Fig. 3d). Three peak regions appear in the distribution of relaxation times (DRT) curves of the CTF anode (Fig. 3e and f). The peaks located at less than $10^{-6.5}$ s correspond to the contact resistance (R_s) between the CTF anode and the current collector. Its intensity decreases slightly during the initial discharging procedure and then stabilizes.[43,44] The peaks that emerged between $10^{-6.4}$ and 10^{-4} s are ascribed to the SEI impedance (R_{SEI}). During the initial discharging, the R_{SEI} exhibits irreversible evolution associated with the formation of the SEI.[43,44] The peaks positioned between 10^{-3} and 10^{-2} s are the charging transfer impedance (R_{ct}) related to the diffusion process and decrease markedly during discharging, indicating that sodiation of CTF facilitates Na^+ diffusion through the electrode.[43,44] Fig. S8 shows the changes in EIS of CTF under different numbers of cycles. It can be observed that the R_{ct} value increases after the first cycle, which is due to the formation of the SEI, and eventually reaches a relatively stable value. To investigate the structure and morphology of the CTF during cycling, *ex situ* SEM characterizations of the electrode before/after cycling and under fully discharged/charged states were performed. As shown in Fig. S9, the pristine CTF exhibits a uniform plate-shaped morphology with clear structural integrity. After 30 cycles, the plate-like structure is well-preserved without obvious pulverization, aggregation, or morphological collapse. Fig. S10 shows that the plate-shaped morphology of CTF is well-preserved in both the fully charged and discharged states. Furthermore, *ex situ* FTIR was carried out in the full sodiation/desodiation state (Fig. S11), and the intrinsic peaks of the triazine group undergo an intensity change, indicating that it is the active storage site in CTF. These results confirm that CTF possesses structural stability during electrochemical cycling.

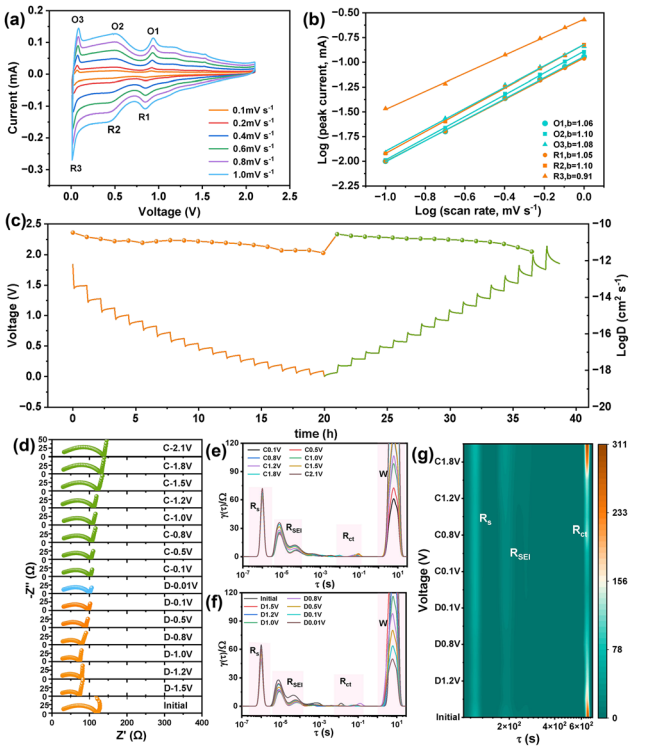

Fig. 3 Kinetic analysis of the CTF anode: (a) CV curves at various scan rates from 0.1 to 1.0 mV s^{-1}. (b) Linear fitting plots of log(i) and log(v) at the redox peaks. (c) GITT profiles and calculated diffusion coefficient of Na^+. (d) *In situ* EIS images of CTF during discharging and charging. (g) DRT profiles of CTF at different voltages. (d) *In situ* EIS spectra, (e) and (f) DRT and (g) DRT contour plots of the CTF anode during the first cycle.

To comprehensively evaluate the electrochemical performance of the CTF anode, the full cells were also assembled. As illustrated in Fig. 4a, the CTF is coupled with the $Na_3V_2(PO_4)_3$ (NVP) cathode and 1 M $NaPF_6$ in ethylene glycol dimethyl ether (DME) as the electrolyte. As shown in Fig. S12, the commercial NVP cathode presents an irregular sheet-like structure, which may provide a large electrode–electrolyte contact area, facilitating the penetration of the electrolyte and the diffusion of Na^+ ions. Fig. 4b exhibits the charge/discharge profiles of the NVP//CTF full cell at 0.1 A g^{-1}, which displays a distinct voltage plateau matching the voltage plateau of CTF and NVP. The cycling behavior in Fig. 4c exhibits that the reversible capacity approximates 93.8 mAh g^{-1} over 110 cycles, indicating favourable cycling stability. Furthermore, the long-term cycling performance was also carried out at a large current density of 1.0 A g^{-1}. As depicted in Fig. 4d, the voltage-capacity curves of the NVP//CTF full cell undergo a certain degree of electrode polarization and capacity decay. Fig. 4e depicts obvious capacity during the initial dozens of cycles, and remained stable to 1579 cycles and delivered 57.6 mAh g^{-1}.

In summary, a covalent triazine framework with a plate shape was obtained *via* a solution synthesis route. As an anode

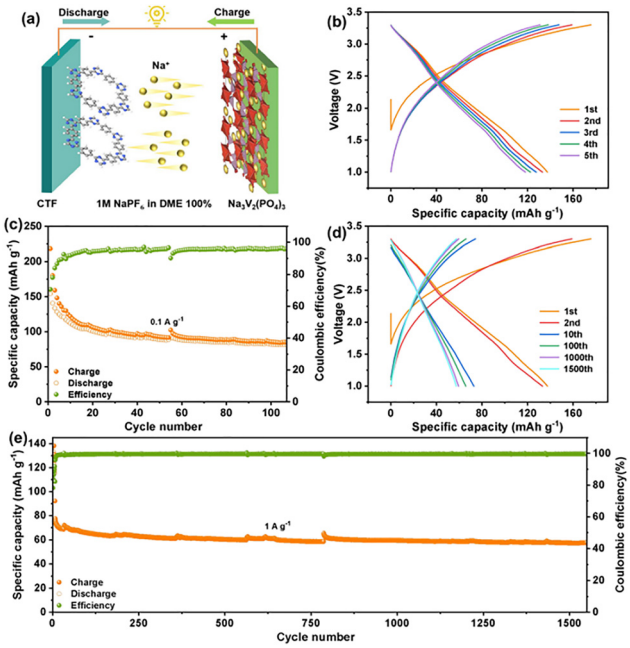

Fig. 4 Electrochemical performance of NVP//CTF full cells. (a) The schematic NVP//CTF full cell. (b) The charge–discharge curves at 0.1 A g^{-1}. (c) Cycling performance at 0.1 A g^{-1}. (d) Charge–discharge profiles from the 1st to 1500th cycles, and (e) corresponding long-term cycling performance at 1.0 A g^{-1}.

for SIBs, this CTF polymer research shows superior rate performance and stable cycling stability. It achieves 82.6 mAh g^{-1} after 9000 cycles at 2.0 A g^{-1}, and retains a specific capacity of 156.8, 141.2, 133.9, 129.0, and 124.9 mAh g^{-1} as the charging/discharging current density from 0.1 to 0.2, 0.5, 1.0, and 2.0 A g^{-1}, respectively. Detailed *in situ* EIS, CV, and GITT analysis for SIBs indicate that the interfacial and superficial pseudocapacitive behaviors occupied the entire cycling process, thereby resulting in superior rate capability. The superior Na-ion storage performance can be ascribed to the extended conjugate structure, which effectively enhances integral electronic conductivity and ensures rapid Na-ion/electron diffusion. This application of CTF materials for SIBs will open an avenue for designing COF materials for energy storage devices, not limited to LIBs, SIBs, and supercapacitors.

Ying Huang and Suping Chen: writing – original draft, investigation, and data acquisition. Fangkun Li, Sihuan Tang, and Yanping Huo: characterizations, conceptualization, and validation. Xijun Xu, Jujun Yuan, and Jun Liu: supervision, funding acquisition, and writing – review and editing.

This research was financially supported by the National Natural Science Foundation of China (No. 52301266 and U21A20332), the Guangdong Basic and Applied Basic Research Foundation (No. 2025A1515012152), the Science and Technology Planning Project of Guangzhou (No. 2024A04J3332), and the Chenzhou National Sustainable Development Agenda Innovation Demonstration Zone Provincial Special Project (No. 2023sfq11). We also thank the Instrumental Analysis Center at Guangdong University of Technology for assistance with the TEM test.

Conflicts of interest

There are no conflicts to declare.

Data availability

The data supporting this article have been included in the supplementary information (SI). The supplementary information file contains detailed experimental procedure, SEM images, and characterization of the material's physicochemical properties, and complementary datasets related to redox reaction mechanisms and electrochemical stability evaluations. See DOI: https://doi.org/10.1039/d5cc07128c.

References

1 P. K. Nayak, L. Yang, W. Brehm and P. Adelhelm, *Angew. Chem., Int. Ed.*, 2018, **57**, 102–120.
2 A. Yao, S. M. Benson and W. C. Chueh, *Nat. Energy*, 2025, **10**, 404–416.
3 X. Xu, F. Li, D. Zhang, S. Ji, Y. Huo and J. Liu, *Carbon Neutralization*, 2023, **2**, 54–62.
4 A. Rudola, R. Sayers, C. J. Wright and J. Barker, *Nat. Energy*, 2023, **8**, 215–218.
5 X. Lu, S. Li, Y. Li, F. Wu, C. Wu and Y. Bai, *Adv. Mater.*, 2024, **36**, 2407359.
6 Y. Gao, H. Zhang, J. Peng, L. Li, Y. Xiao, L. Li, Y. Liu, Y. Qiao and S. L. Chou, *Carbon Energy*, 2024, **6**, e464.
7 Q. Wang, D. Zhou, C. Zhao, J. Wang, H. Guo, L. Wang, Z. Yao, D. Wong, G. Schuck and X. Bai, *Nat. Sustainability*, 2024, **7**, 338–347.
8 Q. Li, X. Xu, J. Tan, H. Sun, J. Zhao and Y. Huo, *J. Energy Chem.*, 2025, **114**, 60–82.
9 X. Fan, X. Kong, P. Zhang and J. Wang, *Energy Storage Mater.*, 2024, **69**, 103386.
10 B. Zhao, G. Suo, R. Mu, C. Lin, J. Li, X. Hou, X. Ye, Y. Yang and L. Zhang, *J. Colloid Interface Sci.*, 2025, **677**, 637.
11 S. Tan, Y. Wen, J. Li, Z. Huang, Z. Zhang, Y. Lai, Z. Tian and S. Li, *Carbon Neutralization*, 2025, **4**, e70071.
12 Z. Chen, L. Yang, G. Yu, R. Yang, Y. Zhao, C. Liu, F. Zhang and Y. Tang, *Energy Storage Mater.*, 2026, **84**, 104745.
13 Y. Wang, X. Xu, Y. Wu, F. Li, W. Fan, Y. Wu, S. Ji, J. Zhao, J. Liu and Y. Huo, *Adv. Energy Mater.*, 2024, **14**, 2401833.
14 R. Shao, Z. Sun, L. Wang, J. Pan, L. Yi, Y. Zhang, J. Han, Z. Yao, J. Li and Z. Wen, *Angew. Chem., Int. Ed.*, 2024, **63**, e202320183.
15 X. Xu, F. Li, D. Zhang, Z. Liu, S. Zuo, Z. Zeng and J. Liu, *Adv. Sci.*, 2022, **9**, 2200247.
16 C. Lin, P. Feng, P. Geng, S. Zhang, Y. Chen, Y. Shen and Y. Zheng, *Chem. Commun.*, 2025, **61**, 16354–16371.
17 J. Mo, X. Xu, J. Tan, W. Fan, J. Zhao, J. Liu and Y. Huo, *Energy Storage Mater.*, 2025, **82**, 104557.
18 T. Yang, X. Xu, Y. Yang, W. Fan, Y. Wu, S. Ji, J. Zhao, J. Liu and Y. Huo, *Energy Mater. Adv.*, 2024, **5**, 0078.
19 S. Chen, X. Xu, T. Yang, W. Fan, J. Zhao and Y. Huo, *Prog. Nat. Sci.: Mater. Int.*, 2025, **35**, 31–50.
20 L. Habib, G. Suo, C. Lin, J. Li, S. Javed, K. Naseem and Z. K. Kalkozova, *Renewable Sustainable Energy Rev.*, 2025, **217**, 115721.
21 Z. Y. Gu, J. M. Cao, K. Li, J. Z. Guo, X. T. Wang, S. H. Zheng, X. X. Zhao, B. Li, S. Y. Li, W. L. Li and X. L. Wu, *Angew. Chem., Int. Ed.*, 2024, **63**, e202402371.
22 W. Li, C. Zhao, C. Yu, Y. Yu, J.-Q. Huang, Y. Lu, H. Jiang, S. Gu, Z. Lu and X. Yang, *Green Energy Environ.*, 2025, **10**, 2201–2258.
23 O. Buyukcakir, J. Ryu, S. H. Joo, J. Kang, R. Yuksel, J. Lee, Y. Jiang, S. Choi, S. H. Lee and S. K. Kwak, *Adv. Funct. Mater.*, 2020, **30**, 2003761.
24 Y. Yu, Q. Jin, Q. Li, H. Sun, Y. Ren, S. Xia, S. Wang and Z. Jin, *Nano Energy*, 2025, **137**, 110808.
25 P. Xiong, S. Zhang, R. Wang, L. Zhang, Q. Ma, X. Ren, Y. Gao, Z. Wang, Z. Guo and C. Zhang, *Energy Environ. Sci.*, 2023, **16**, 3181–3213.

26 Y. Zheng, N. A. Khan, X. Ni, K. A. Zhang, Y. Shen, N. Huang, X. Y. Kong and L. Ye, *Chem. Commun.*, 2023, **59**, 6314–6334.
27 J. Aslam, M. A. Waseem, X. M. Lu, S. Wu, W. Sun and Y. Wang, *Small*, 2025, **21**, 2408988.
28 Z. Wang, X. Zou, M. Lv and B. Zhang, *Energy Mater.*, 2024, **4**, 400072.
29 J. Liu, W. Zan, K. Li, Y. Yang, F. Bu and Y. Xu, *J. Am. Chem. Soc.*, 2017, **139**, 11666–11669.
30 S. Ren, M. J. Bojdys, R. Dawson, A. Laybourn, Y. Z. Khimyak, D. J. Adams and A. I. Cooper, *Adv. Mater.*, 2012, **24**, 2357–2361.
31 R. Zhuang, X. Zhang, C. Qu, X. Xu, J. Yang, Q. Ye, Z. Liu, S. Kaskel, F. Xu and H. Wang, *Sci. Adv.*, 2023, **9**, eadh8060.
32 K. Wang, L. M. Yang, X. Wang, L. Guo, G. Cheng, C. Zhang, S. Jin, B. Tan and A. Cooper, *Angew. Chem., Int. Ed.*, 2017, **56**, 14149–14153.
33 C. Li, A. Yu, X. Chen, T. He, S. Mei, G. Long and C.-J. Yao, *Chem. Eng. J.*, 2024, **489**, 151103.
34 S.-Y. Li, W.-H. Li, X.-L. Wu, Y. Tian, J. Yue and G. Zhu, *Chem. Sci.*, 2019, **10**, 7695–7701.
35 Z. Liu, C. Wang, W. Yuan and Y. Xu, *Chin. J. Chem.*, 2024, **42**, 301–316.
36 J. Liu, P. Lyu, Y. Zhang, P. Nachtigall and Y. Xu, *Adv. Mater.*, 2018, **30**, 1705401.
37 B. Ball, C. Chakravarty and P. Sarkar, *J. Phys. Chem. C*, 2019, **123**, 30155–30164.
38 J. Zhang, X. Fu, J. Qiu, C. Wang, L. Wang, J. Feng, L. Dong, C. Long, X. Wang and D. Li, *Adv. Sci.*, 2024, **11**, 2401804.
39 D. Chao, R. DeBlock, C. H. Lai, Q. Wei, B. Dunn and H. J. Fan, *Adv. Mater.*, 2021, **33**, 2103736.
40 D. Chao, C. Zhu, P. Yang, X. Xia, J. Liu, J. Wang, X. Fan, S. V. Savilov, J. Lin and H. J. Fan, *Nat. Commun.*, 2016, **7**, 12122.
41 J. Wang, E. Pameté, S. Yan, W. Zhao, J. Zhang, X. He, Z. Supiyeva, Q. Abbas and X. Pan, *Electrochem. Commun.*, 2023, **150**, 107488.
42 X. Xu, S. Chen, F. Li, P. Zhang, Y. Huo and J. Liu, *Chem. Eng. J.*, 2025, **524**, 169267.
43 S. Zhou, Z. Sun, Z. Zhuang, S. Wen, H. Chen, Q. Yin, J. Pan, X. Chen, J. Xu and Q. Zhang, *Sci. China Mater.*, 2025, **68**, 868–878.
44 K. Ren, H. Zhou, D. Zhang, D. Yang, F. Li, X. Zhang, P. Liu, Y. Zhou, P. Dong and X. Feng, *Adv. Energy Mater.*, 2025, **15**, e00472.